# SEISMIC CHARACTERIZATION OF SUBMARINE GAS-HYDRATE DEPOSITS IN THE WESTERN BLACK SEA BY ACOUSTIC FULL-WAVEFORM INVERSION OF OBS DATA

*L. Gassner, T. Gerach, T. Hertweck and T. Bohlen*

**email:** *Laura.Gassner@kit.edu*

**keywords:** *Ocean-bottom, Hydrate, Full waveform, Inversion, Seismics*

**ABSTRACT**

*Evidence for gas-hydrate occurrence in the Western Black Sea is found from seismic measurements revealing bottom-simulating reflectors (BSRs) of varying distinctness. From an ocean-bottom seismic data set low-resolution traveltime-tomography models of P-wave velocity $v_P$ are constructed. They serve as input for acoustic full-waveform inversion (FWI) which we apply to derive high-resolution parameter models aiding the interpretation of the seismic data for potential hydrate and gas deposits. Synthetic tests show the applicability of the FWI approach to robustly reconstruct $v_P$ models with a typical hydrate and gas signature. Models of S-wave velocity $v_S$ containing a hydrate signature can only be reconstructed when the parameter distribution of $v_S$ is already well known. When we add noise to the modelled data to simulate field data conditions, it prevents the reconstruction of $v_S$ completely, justifying the application of an acoustic approach. We invert for $v_P$ models from field-data of two parallel profiles of 14 km length with a distance of 1 km. Results show a characteristic velocity trend for hydrate and gas occurrence at BSR depth in the first of the analyzed profiles. We find no indications for gas accumulations below the BSR on the second profile and only weak indications for hydrate. These differences in $v_P$ signature are consistent with reflectivity behavior of the migrated seismic streamer data of both profiles where a zone of high reflectivity amplitudes is coincident with the potential gas zone derived from the FWI result. Calculating saturation estimates for the potential hydrate and gas zones yields values of up to 30 % and 1.2 %, respectively.*

## INTRODUCTION

Gas-hydrate deposits store huge amounts of natural gas, and can be found at all continental margins and in permafrost regions. Their stability is controlled by temperature and pressure conditions, and the availability of gas and water. When uprising gas enters the stability zone, hydrate forms and restricts the pathway for further gas migration (Kvenvolden, 1993). Hydrate and gas have distinctive elastic properties, and can therefore be detected with seismic imaging methods. A hydrated sediment layer is typically indicated by an elevated P-wave velocity $v_P$ compared to hydrate-free sediment, and is bound by a sharp $v_P$ decrease below, where the hydrate-stability zone ends. The identification of possible gas-hydrate sites is therefore achieved by the detection of bottom-simulating reflectors (BSRs), which result from this characteristic $v_P$ behavior. Because the BSR depth depends on the stability conditions it is not necessarily coincident with a lithological boundary. It is mostly of high amplitude and of opposite polarity compared to the seafloor reflection. The acquisition of seismic reflection data is therefore the simplest method to identify possible gas-hydrate sites. To quantify the volume of available hydrate, detailed parameter-distribution models need to be derived.

To obtain reliable seismic velocity information of the subsurface, long-offset data are required. Therefore, in most surveys ocean-bottom seismic (OBS) measurements are performed to provide input for velocity analysis. Conventionally, refracted-wave first arrivals are used for traveltime tomography, yielding $v_P$ models which represent a long-wavelength trend of the subsurface parameter distribution. Detailed structures in the range of tens of meters, necessary to map potential gas-hydrate deposits, cannot be resolved using traveltime-based methods. To improve the resolution of subsurface models, full-waveform inversion (FWI) is applied. The concept of acoustic FWI was introduced by Tarantola (1984), and an elastic formulation by Mora (1988). In theory, multiparameter images of the subsurface can be obtained in great detail (e.g. Sears et al., 2008), provided that simulated and measured traveltimes match within half a wavelength for a starting parameter model (Virieux and Operto, 2009).

First FWI studies aiming at gas-hydrate characterization were performed with an acoustic approximation in 1D (Singh et al., 1993; Pecher et al., 1996; Korenaga et al., 1997). They were able to derive $v_P$ signatures with elevated velocity by up to 300 m/s above and a velocity drop of 600 m/s at BSR depth. A 2D acoustic FWI approach was applied to multichannel seismic (MCS) data by Delescluse et al. (2011), associating increased velocities with a gas-hydrate zone and low-velocity zones with the occurrence of gas. They conclude that the acoustic approximation is valid also for far-offset data, provided $v_S$ is varying smoothly with depth. Kim et al. (2013) show results of 2D elastic FWI, where they observe increased P- and S-wave velocities as well as a reduced poisson ratio in a zone related to hydrate occurrence. An underlying layer of decreased velocity and higher poisson ratio is interpreted as a gas zone. Jaiswal et al. (2012) perform visco-acoustic 2D FWI and relate increased velocities as well as reduced attenuation to the presence of gas hydrate, and reduced velocities and increased attenuation to gas occurrence. In contrast to these results, laboratory measurements indicate increased attenuation in hydrated sediments (Guerin and Goldberg, 2002).

While all FWI studies mentioned in the previous paragraph involve the use of MCS data, we demonstrate that local gas and hydrate distribution in marine sediments can also be explored by the inversion of OBS data. Although only few stations are available, the approach is advantageous in terms of computing time, as we can apply the reciprocity principle. OBS locations serve as virtual source positions, and the actual shot locations as virtual receiver positions. Despite the low coverage it is still possible to identify potential gas-hydrate accumulations. In this paper, we first describe the applied FWI approach, and then introduce the measurement area and the field data. Synthetic studies give an insight into the resolution capability of acoustic and elastic FWI for the available geometry and data quality. We show results of acoustic field-data inversion for two profiles and compare two different time-windowing approaches, one with all events and one with muted input data disregarding the direct waves and primary reflections. Finally, we link recovered parameter distribution to potential hydrate and gas concentration.

## FWI APPROACH

To study the subsurface parameters along the recorded seismic profiles we apply a 2D time-domain full-waveform inversion approach (Köhn, 2011). For a chosen starting model, synthetic seismograms are computed by the finite-difference (FD) method (Virieux, 1986). For each shot an initial misfit $E$ is calculated between synthetic seismograms $s$ and corresponding field data $d$. A standard $L_2$-norm is used for the misfit definition, according to

$$E(\mathbf{m}) = \sum_{r=1}^{n_r} \int_0^T \left(s(\mathbf{x}_s, \mathbf{x}_r, \mathbf{m}, t) - d(\mathbf{x}_s, \mathbf{x}_r, t)\right)^2 dt \tag{1}$$

where $n_r$ equals the number of receivers and $T$ the recording time. Source and receiver positions are denoted by $\mathbf{x}_s$ and $\mathbf{x}_r$, respectively. The subsurface model $\mathbf{m}$ is parametrized by the seismic velocities and the density $\rho$, with $\mathbf{m} = (v_P, v_S, \rho)$ for an elastic approach, and $\mathbf{m} = (v_P, \rho)$ in the acoustic approximation. Steepest-descent parameter gradients $\frac{\partial E}{\partial \mathbf{m}}$, according to the adjoint method (Plessix, 2006), are calculated from the cross-correlation of forward-propagated wavefields with corresponding back-propagated residual wavefields. To update each parameter model, a conjugate-gradient approach is used.

To find an optimal step length $\alpha$, a parabolic fitting method is applied to a set of calculated test step lengths (Kurzmann, 2012). The inversion is executed until the misfit can no longer be decreased significantly.

At each iteration $n$ the model $\mathbf{m}$ is updated by

$$\mathbf{m}_{n+1} = \mathbf{m}_n - \alpha_n \mathbf{P}_n \frac{\partial E(\mathbf{m}_n)}{\partial \mathbf{m}}. \tag{2}$$

To improve the convergence of the inversion, preconditioning by a chosen operator $\mathbf{P}$ can be applied. We apply three types of preconditioning, a) tapering of the water column, i.e., no update is applied in this area, b) a radial taper at the source (OBS) positions, and c) a weighting that reduces effects of geometrical spreading of seismic data (Plessix and Mulder, 2004). Tapers b) and c) are applied shotwise. Additionally, a horizontal smoothing filter is applied to reduce horizontal parameter oscillations.

In order to reduce the non-linearity of the inverse problem, low-pass filtering is applied to gradually increase the frequency content of the input data. Additionally, we apply high-pass filtering in the case of prominent low-frequency noise, which is often present in marine field data. For 2D field-data inversion a correction for the 3D propagation characteristics is necessary, and we apply the geometrical-spreading correction suggested by Forbriger et al. (2014) which is valid for reflected waves: convolution of each trace with $1/\sqrt{t}$ ($t$: traveltime) and a multiplication by $v\sqrt{2t}$ ($v$: velocity). To account for the unknown source signature of the recorded data, a correction filter is derived at the beginning of each frequency stage by a stabilized deconvolution (Groos et al., 2014). The signature of the main events in the field data and in the modeled seismograms of the starting model is thereby adjusted, and further adjustment is reached by the repeated inversion of a source time function (STF) after adding more frequency content to the general inversion process.

As the emitted energy for different shots can vary, also the signal amplitude of traces can differ along a seismic profile. Therefore, Choi and Alkhalifah (2012) suggest to apply a weighting by the corresponding RMS-amplitude to each seismic trace of field data. This also reduces the influence of geometrical amplitude loss, and allows far-offset data to equally contribute to the misfit. A drawback of this approach is that the sensitivity for a potential inversion of attenuation is lost. Nevertheless, attenuation can be incorporated as a passive parameter, and can be accounted for by providing models of the quality factor $Q$ (Bohlen, 2002).

## FIELD DATA

Regions of BSR occurrence were identified in the Western Black Sea from regional MCS data, acquired with cruise MSM34 in 2013/2014 (Bialas et al., 2014). In an area of approximately 160 km$^2$, further high-resolution MCS data were recorded, as well as OBS data to provide far-offset data for velocity analysis. Shots were triggered every five seconds with a 45/45 in$^3$ GI gun seismic source, resulting in a shot spacing of approximately 10 m. In the study area fifteen OBS stations were deployed in a $3 \times 5$ grid, with 1 km distance between stations. Stations were equipped with hydrophones and 3-component geophones. The measurement was arranged such that three profiles (P1 to P3) of 14 km length covering five stations each are orientated along a channel axis, and five profiles (P4 to P8) of approximately 11 km length lie perpendicular (Figure 1).

Due to a nearby industrial seismic survey, data starting at the end of profile P2 are superimposed by strong signals at frequencies below 30 Hz. Therefore, we concentrate on profiles P1 and P2 for the application of FWI. Also, geophone data show high noise levels in the low-frequency range in general, which is why we focus on hydrophone data for field-data FWI. Because of sea currents OBS stations are located up to 100 m away from the respective profile lines.

As one common analysis approach of the OBS data is traveltime tomography of refracted-wave first arrivals, the amplification of the recorded seismic signals was chosen high in order to identify wave onsets best. This partly leads to clipping of the short-offset direct-wave arrivals. Additionally, we observe strong ringing, also following the direct-wave arrival which masks most of the primary reflections. Within the multiply reflected waves a signal related to the BSR is visible following the multiple of the direct wave arrival after approximately 0.5 s. A potential reflection of the BSR is not visible within the primary reflections. We therefore consider the application of time-windowing during FWI to mute the direct wave and primary reflections. In a first test we invert all events and then mute the input data so that only refracted waves and multiple reflections are used in a second test (compare Figure 2). As a preparation for inversion 3D-to-2D transformation is applied to the data of both profiles, using the sound velocity of the water column. Frequency analysis shows that the 3D-to-2D correction filter strongly increases low-frequency noise. Therefore, a high-pass filter at 5 Hz is applied during inversion.

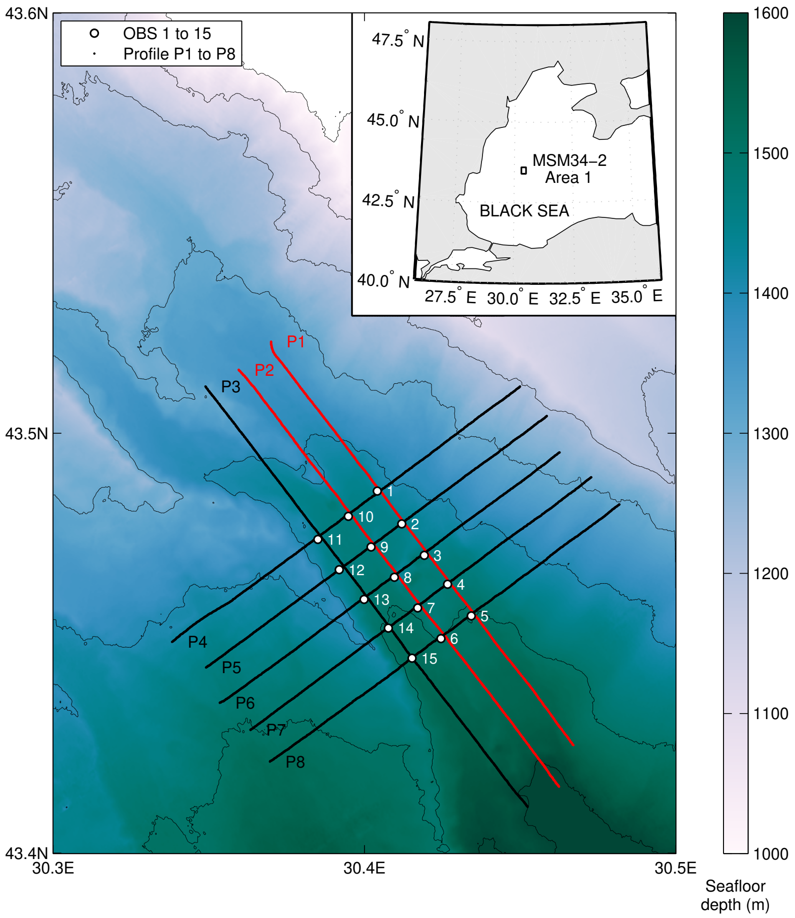


**Figure 1:** Map of the study area bathymetry with the geometry of high-resolution seismic and OBS measurements. OBS stations are represented by white circles and seismic profiles by black lines. Hydrophone data of profiles P1 and P2, which are used for FWI, are marked in red. The inset shows the location of the study area in the Western Black Sea.

Analysis of the BSR signature from high-resolution MCS data suggests that a sharp BSR signal is present for a large segment of profile P1, while at profile P2 a weaker signature is observed. For a detailed analysis of the BSR distribution in the measurement area we refer to Zander et al. (2017).

## SYNTHETIC STUDY

We conduct synthetic inversion tests to examine the general applicability of acoustic and elastic FWI to recover seismic velocities, relatable to hydrate and gas occurrence, with the configuration of our survey. For the geometry of profile P2, we construct a model with a typical BSR signature (Figure 3), and calculate pseudo-observed data by applying elastic modeling. To simulate field-data quality, we add Gaussian noise to the calculated data for a further test.

For the construction of the parameter models we utilize horizons from the interpretation of depth-migrated streamer data, and seismic velocities from traveltime analysis of the OBS data. On top of a background model with increasing layer velocity with depth, we add an increase in $v_P$ above the BSR of up to 300 m/s and a decrease of the same value below (Figure 3a). A $v_S$ model (Figure 3b) is constructed by assuming a decreasing $v_P/v_S$ ratio of 3 at the seafloor to 2 at the bottom of the model. Hydrate accumulation above the BSR horizon is assumed to increase $v_S$ by 200 m/s compared to the background model, while below the BSR $v_S$ remains unchanged. Density values (Figure 3c) are calculated by the application of the

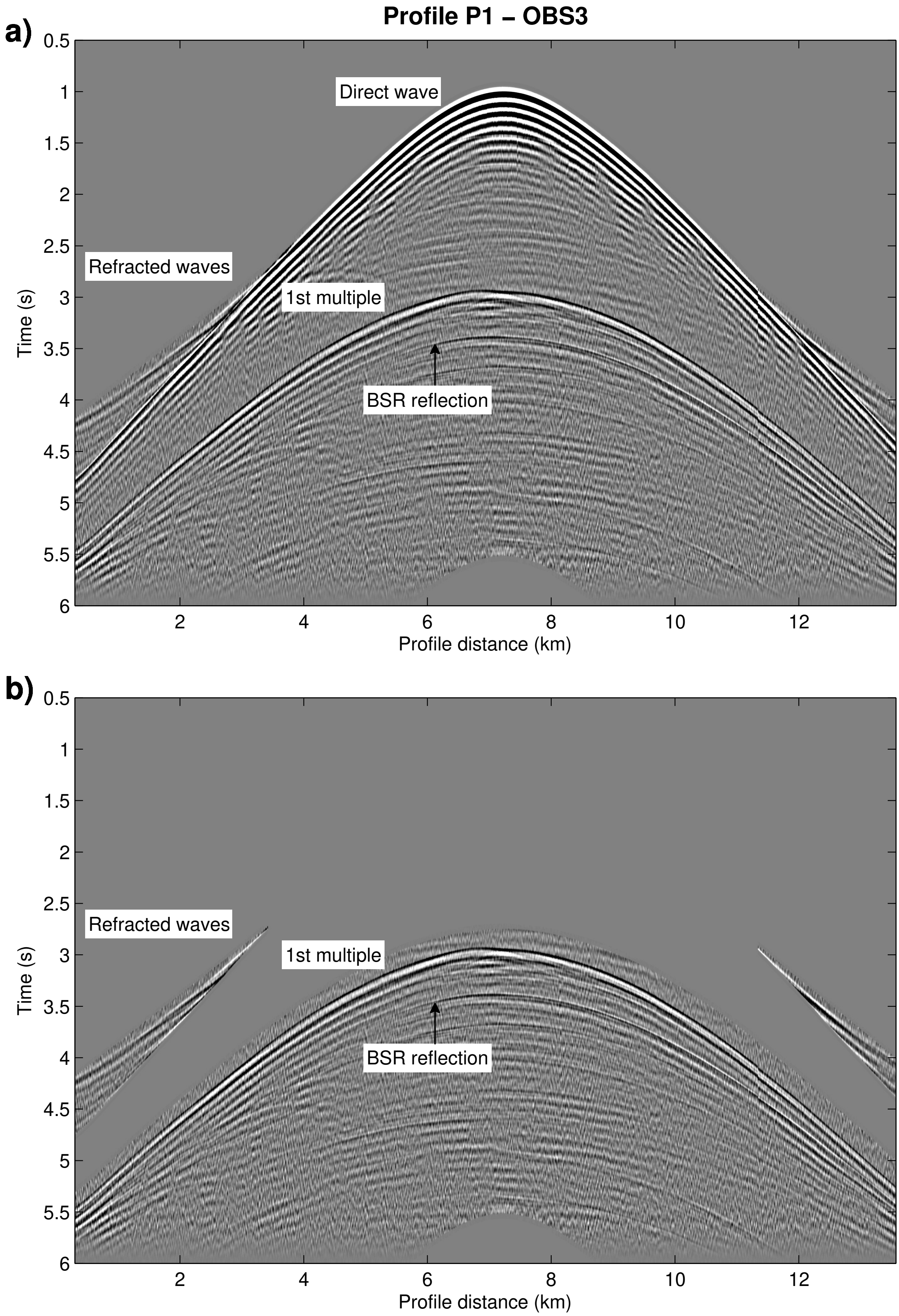


**Figure 2:** Preprocessed hydrophone data of OBS 3 at profile P1 serving as input for FWI. (a) All events with a mute before the first arrival and (b) muted input data without the direct wave and primary reflections.

Gardner relation (Gardner et al., 1974) to the background $v_P$ model. In the density model no effect of hydrate and gas on the parameter values are assumed.

To obtain a starting model for the synthetic tests, we apply Gaussian smoothing to the constructed parameter models. The resulting models include no information on the horizons or the BSR velocity contrast, and are in smoothness similar to a model obtained by traveltime tomography (Figure 3d). We perform inversion tests, applying acoustic and elastic inversion to the original elastic data, and elastic inversion to data where Gaussian noise was added. A signal-to-noise ratio (SNR) of eight agrees well with field-data quality. The frequency content of the inverted data is increased in steps of 5 Hz starting with a low-pass filter at 5 Hz, and at 10 Hz for noisy data. At the final stage we use frequencies up to 25 Hz. Additionally, a high-pass filter at 3 Hz is applied in the inversion of noisy data. At the first frequency stage we start with inversion for $v_P$ only, and then add inversion for $v_S$ and $\rho$ successively, while in the later stages all parameters are inverted for simultaneously. In the synthetic studies the misfit is calculated by a standard $L_2$-norm without seismogram normalization.

The application of acoustic inversion to noise-free elastic data leads to a successful reconstruction of the BSR signature in the $v_P$ model (Figure 4b). Between 2 km and 12 km profile distance, the velocity maximum above the BSR horizon is resolved on average with 100 m/s less than the true value, and the velocity minimum within 100 m/s. While the BSR horizon is clearly visible in the inversion result, horizons above and below are hardly discernable. At the OBS positions vertically orientated structures appear below the BSR. The reconstructed density model shows strong fluctuations, which serve to compensate for lacking S-wave information. Also, near the seafloor large parameter changes are visible.

Elastic inversion allows for a good recovery of both BSR signatures in $v_P$ and $v_S$ (Figure 5). In this case the $v_P$ maximum and minimum, above and below the BSR, respectively, are reconstructed within 50 m/s of the true values between 2 km and 12 km profile distance (Figure 5a). The absolute velocity contrast is slightly overestimated. The $v_S$ increase above the BSR can be resolved within 50 m/s between 3 km and 11 km profile distance (Figure 5b). Further horizons are clearly discernable above the BSR, and can also be determined below. Again, vertical artifacts are present in the $v_P$ model below BSR depth, though with noticeably reduced amplitude compared to the acoustic inversion result. Parameter fluctuations are much weaker in the inverted density model, but still higher than contrasts in the true model.

When we invert noise-contaminated elastic data, we are still able to resolve the BSR signature in $v_P$ (Figure 6a). The maximum P-wave velocity above the BSR is reconstructed within 200 m/s, and the minimum velocity below the BSR within 100 m/s. Overall, the $v_P$ contrast is underestimated by approximately 100 m/s. Horizons above the BSR are still discernable in $v_P$. In the $v_S$ model (Figure 6b), neither the BSR signature nor any horizons are resolved. The inverted density model shows similar fluctuations as in the result from the inversion of noise-free data.

From these tests we find that under field-data conditions, e.g. the presence of noise, we are not able to gain information on the $v_S$ distribution. Variations in the density model could not be reconstructed with any test setting, while the BSR signature in $v_P$ could be reconstructed robustly in all examined cases. Although in general the elastic inversion outperforms the acoustic result, further tests also show that a $v_S$ starting model closely following the velocity trend is necessary to obtain the correct $v_S$ distribution at BSR depth. A less accurate $v_S$ starting model increases vertical artifacts and decreases general resolution.

Furthermore, the application of muting of the direct wave and primary reflections as suggested for the field data proved to have negligible effect on the inversion result (not shown). We conclude that an acoustic approach is sufficient to achieve an interpretable $v_P$ inversion result for the available field data as we do not have reliable information on the $v_S$ distribution and observe a significant level of noise in the data.

## FIELD DATA INVERSION

Starting models of $v_P$ for field data inversion are created from the results of traveltime tomography using refracted-wave first arrivals (Figure 7). The resulting parameter models are limited by ray coverage to the extent of the shot positions and in depth to 3 km below the OBS stations. They are then extrapolated to an equidistant grid covering 14.4 km length, with a grid spacing of 2 m to satisfy spatial FD discretization criteria. In the water column we assume a constant velocity of 1484 m/s and a density of 1020 kg/m$^3$, which we find to reflect Black Sea conditions best. Velocity values in the sediment column range from 1500 m/s to 2500 m/s at 3 km depth. A density model is calculated by the Gardner relation, yielding

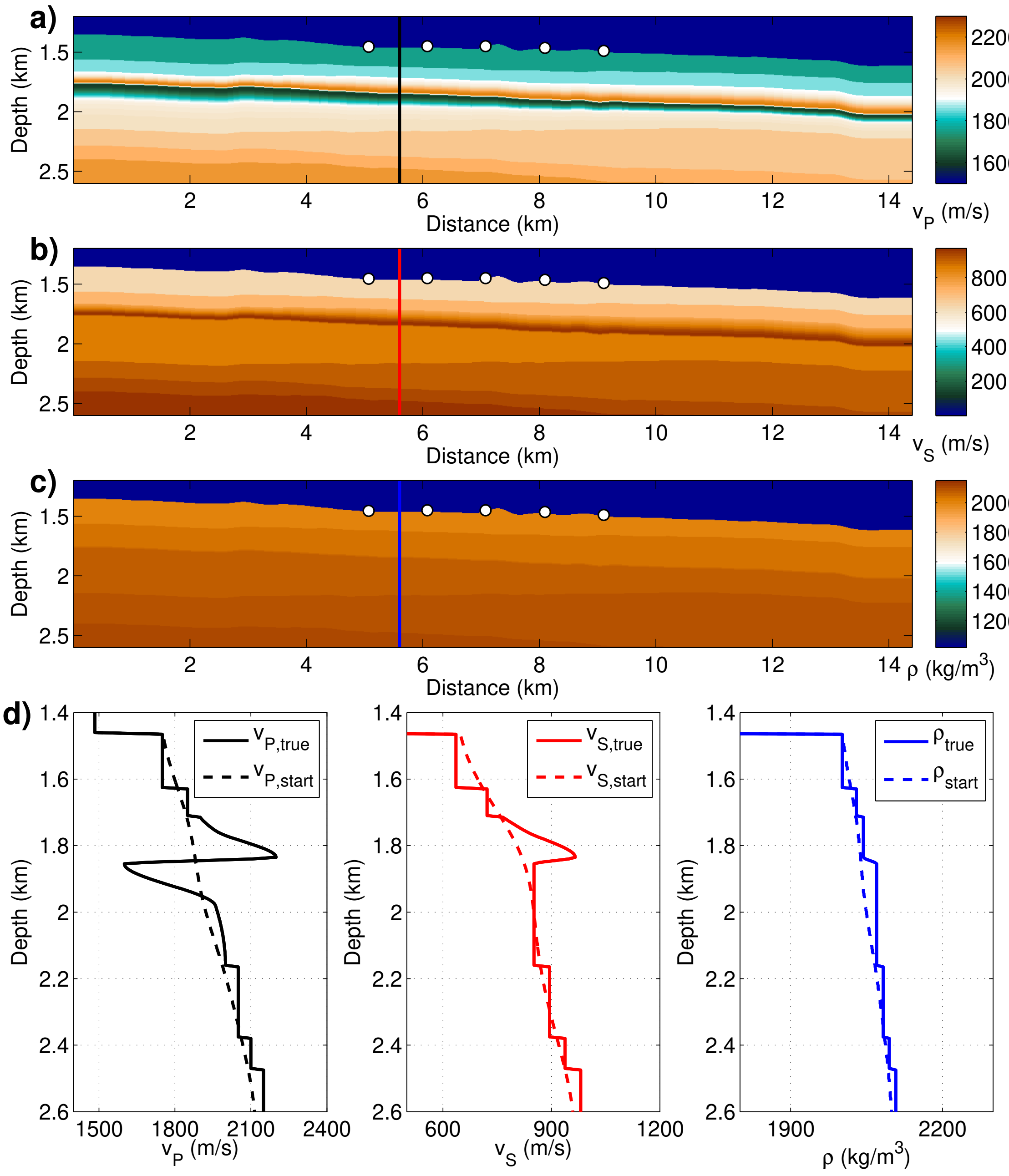


**Figure 3:** (a) True $v_P$, (b) $v_S$ and (c) $\rho$ models for the synthetic study using the geometry of profile P2. (d) Depth profiles of the models at a profile distance of 5.6 km with depth profiles of the starting models at the same location.

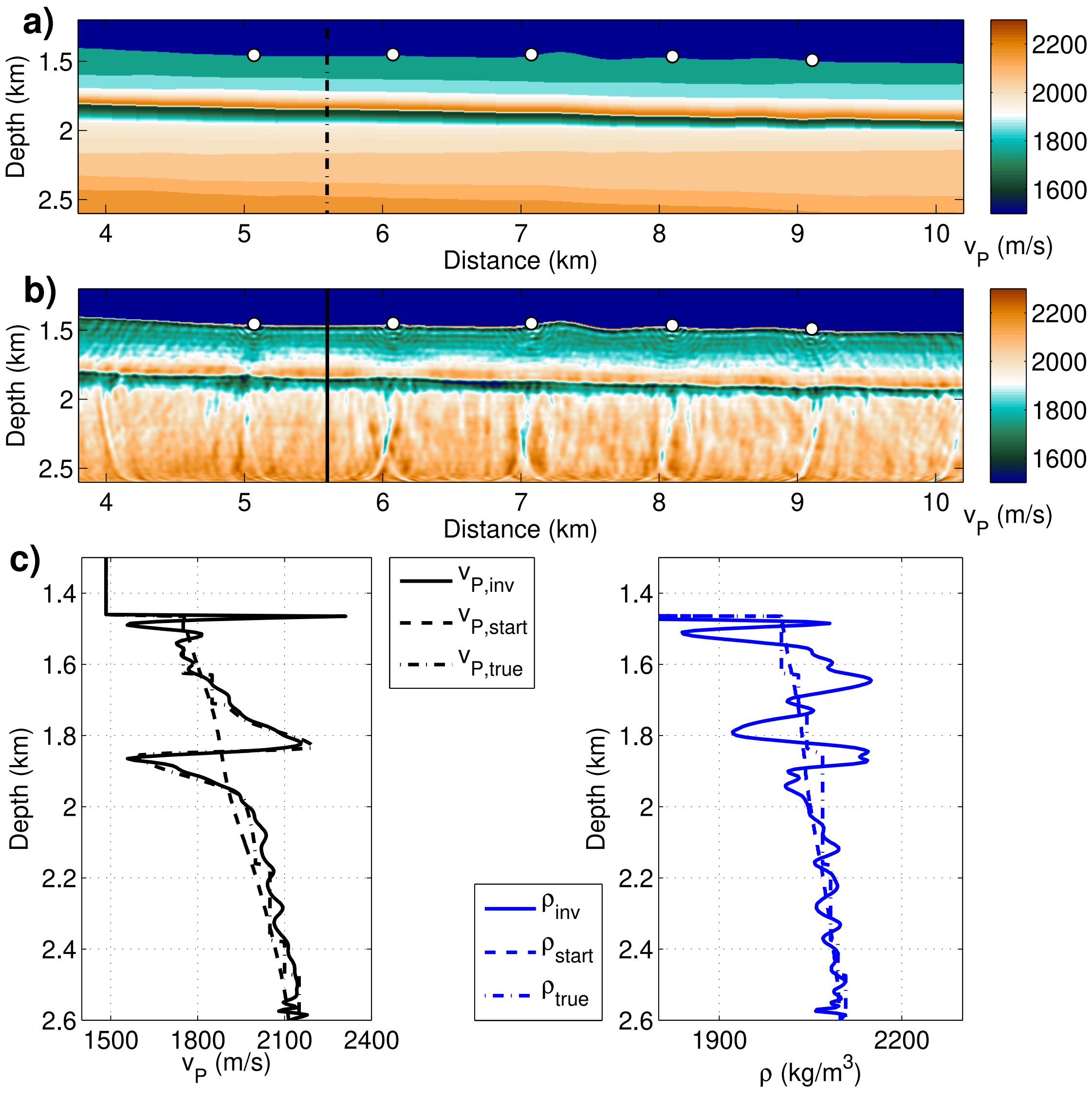


**Figure 4:** (a) True and (b) inverted $v_P$ model for the synthetic study using acoustic FWI on noise-free elastic data. (c) Depth profiles of inverted $v_P$ and $\rho$ models at a profile distance of 5.6 km.

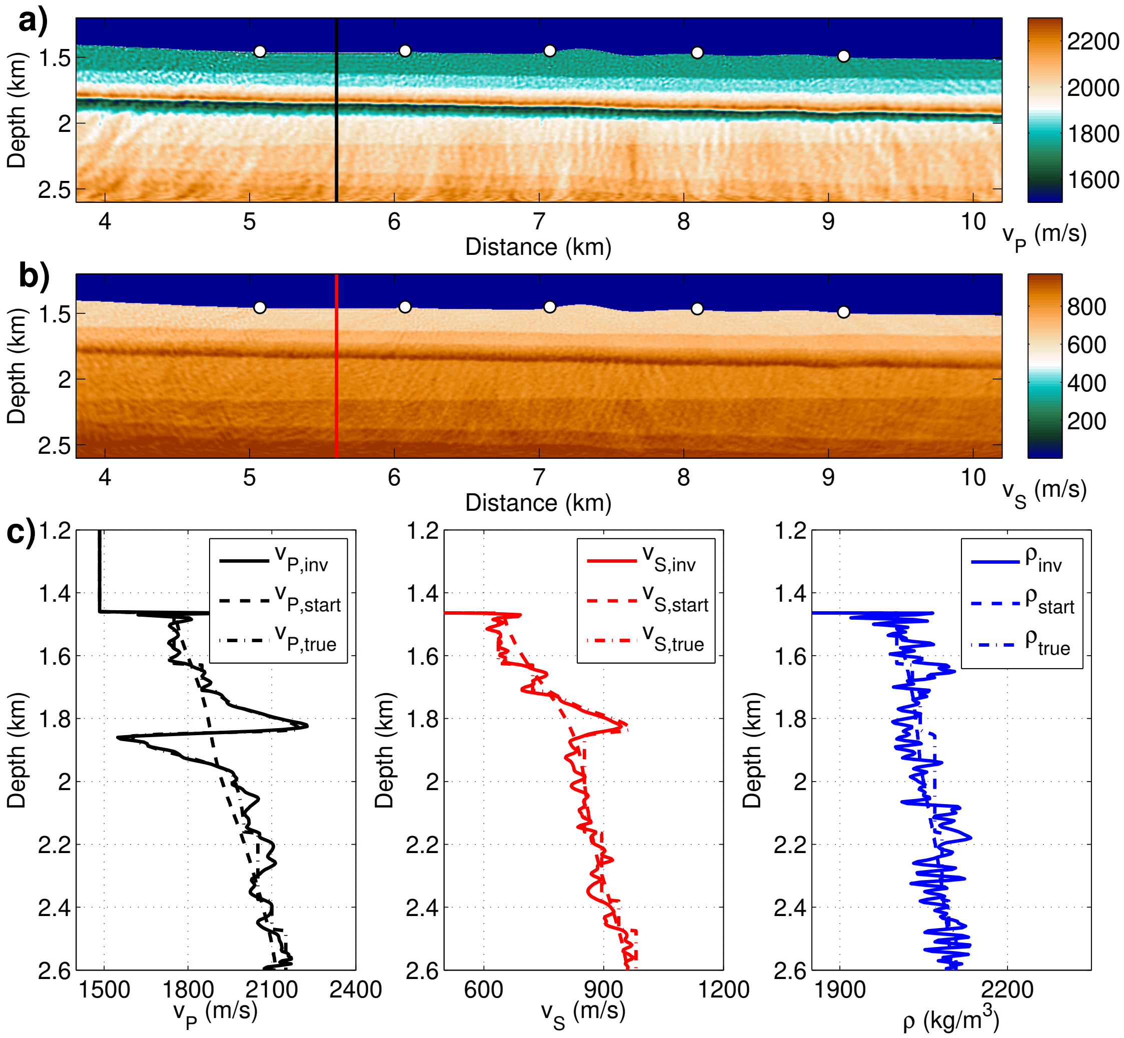


**Figure 5:** (a) Inverted $v_P$ and (b) $v_S$ models for the synthetic study using elastic FWI with noise-free data. (c) Corresponding depth profiles of the inverted $v_P$, $v_S$, and $\rho$ models at a profile distance of 5.6 km.

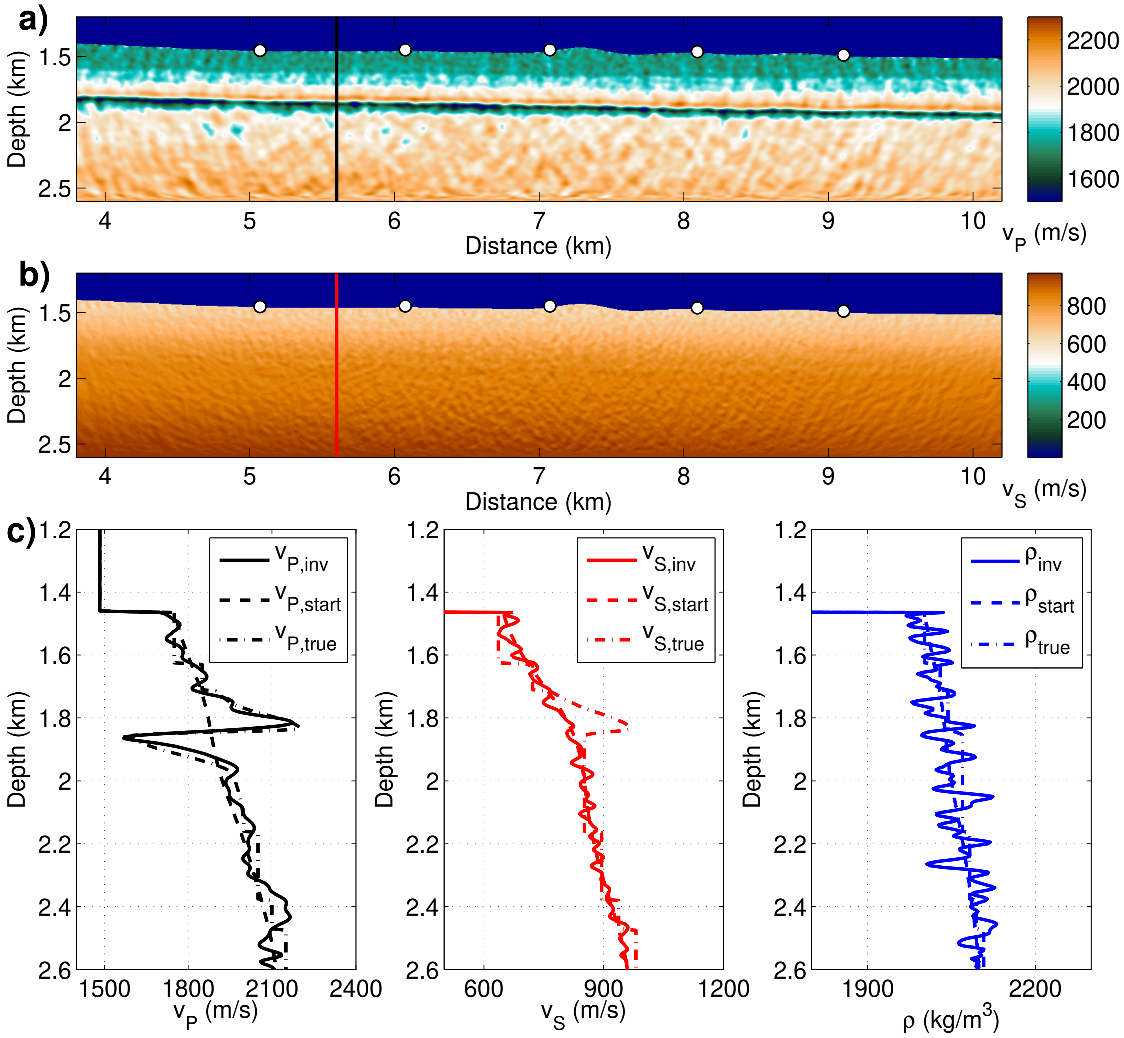


**Figure 6:** (a) Inverted $v_P$ and (b) $v_S$ models for the synthetic study using elastic FWI with noisy data (SNR=8). (c) Corresponding depth profiles of the inverted $v_P$, $v_S$, and $\rho$ models at a profile distance of 5.6 km.

values of 1950 kg/m$^3$ to 2170 kg/m$^3$. To simulate attenuation we assume a constant Q-factor of 100 in the sediments which explains the maximum-amplitude decay with offset well.

For field-data inversion we choose to increase the frequency content from up to 10 Hz in the first stage to 15 Hz and 20 Hz in the second and third stage, respectively, and finally to 30 Hz in the last stage. Furthermore, we now use a normalized $L_2$ norm for the misfit definition and invert for $v_P$ and $\rho$ simultaneously.

## Results

Inverted $v_P$ models show significantly more detail than the initial tomography models, with more pronounced layers and smaller-scale velocity structures. The resulting $v_P$ models from the inversion with all events are shown in Figure 8 for profile P1 and Figure 9 for profile P2. At most of the OBS stations circular structures are constructed by FWI, dominating the upper 200 mbsf (meters below seafloor). We suggest that the deviation of the OBS locations from the 2D geometry is the dominant influence on the amplitude of these structures and errors are projected into the model close to the stations. In the deeper model part a layer of increased velocity, together with a layer of reduced velocity below, is constructed on profile P1 at a depth of 400 mbsf. Both zones extend from 6.5 km to approximately 12 km profile distance where no more significant updates are introduced to the model. The velocity contrast associated with these layers is on average 150 m/s with a maximum of 200 m/s. The average vertical extent of the high- and low-velocity layers is approximately 80 m and 55 m, respectively. In contrast to profile P1 no prominent low-velocity zone at BSR depth is observed on profile P2. A consistent velocity increase of 100 m/s on average is constructed by FWI above the observed BSR horizon.

Inversion results with muted input data (Figure 2b) do not show circular artifacts as observed in the results from inverting all events. Because of the more complex wavepaths of the multiple reflections errors in the OBS locations have a significantly lower impact on the result compared to considering the direct wave arrivals. This results in a better resolution of the shallow subseafloor region. We observe shallow low-velocity zones at around 100 mbsf on both profiles. The overall model differences of the inverted $v_P$ and the starting models are up to 200 m/s while the most significant model changes occur in the upper 200 mbsf or again at BSR depth. On profile P1 shallow reduced velocity zones are visible between 5.5 km and 8 km profile distance at a depth of 100 mbsf (Figure 10). In these zones $v_P$ is reduced by up to 150 m/s. Shallow low-velocity zones appear as patches between 7 km and 9 km profile distance at 100 mbsf at profile P2 (Figure 11). A prominent zone is observed at 200 mbsf between 5 km and 6 km profile distance where velocities are reduced by up to 150 m/s compared to the starting model. The vertical extent of the high- and low-velocity layers on profile P1 is now approximately 70 m and 45 m, respectively

The same patterns recovered in the $v_P$ models also become apparent in the density models. The size of parameter variations with depth are comparable in both results. Deviations in density compared to the starting models are up to 150 kg/m$^3$ in the deeper model region, and up to 200 kg/m$^3$ in the upper 200 m. Simultaneous inversion of $\rho$ and $v_P$ proved to be beneficial for the reduction of strong parameter oscillations with depth appearing in the $v_P$ model at the seafloor.

Synthetic seismograms for the final FWI models using all events are shown in Figure 12. They exhibit a strong similarity with the observed seismograms (Figure 2) although noticeably there are diffraction signals visible which do not occur in the field data. A trace comparison shows a good agreement of the direct wave signal at 0 km offset with weaker similarity at 3.8 km offset. Signals match within the applied time windows as well as for the neglected direct-wave signals when using the muted input data (Figure 13). A stronger mismatch between the synthetic and observed direct wave signature is visible. The match between the multiply reflected signals is improved compared to the result from using all events.

A good agreement of the STF amongst each other can be observed when inverting all events (Figure 14). Stations where stronger artifacts around the OBS stations show in the inverted $v_P$ model exhibit less ringing in the STF than the other stations. A higher similarity of the recovered STF is obtained for both profiles when using the muted input data (Figure 15), with the exception of OBS 10 where an increased noise level is observed in the data compared to the other stations. The onset of STF signals varies slightly for different stations which is related to varying OBS distances perpendicular to the profile. The misfit can be reduced smoothly for all frequency stages in both applications, though no significant decrease can be achieved in the later frequency stages. Eventually, approximately 20 iterations are executed in the inversion of both profiles.

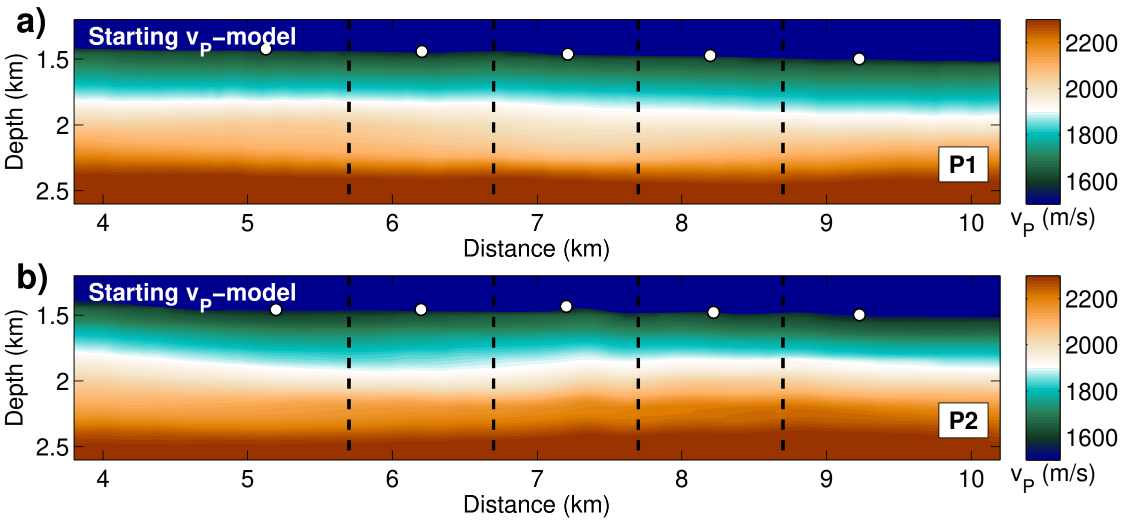


**Figure 7:** Initial $v_P$ models resulting from traveltime tomography of refracted wave first arrivals used for the application of acoustic FWI to field data. (a) Profile P1 and (b) profile P2.

### Evaluation

The $v_P$ models recovered from the muted input data are used for further analysis because they show significantly less artifacts. They are related to the corresponding migrated seismic sections to examine the plausibility of the inverted structures (Figure II and II). Reflectivity behavior visible in seismic streamer data differs strongly between profiles P1 and P2. At profile P1 we observe a clear horizontal layering in the first 200 mbsf and less structure beneath, up to a layer of approximately 60 m thickness. This layer is characterized by parallel high-reflectivity amplitudes and is starting at a profile distance of 6 km continuing up to 10 km. Down to 2.2 km depth we observe additional layered structures of weaker amplitude. At profile P2 the upper 200 m are characterized by more chaotic reflectivity patterns with a clear horizon visible at 200 mbsf. Intermediate reflectivity amplitudes without discernable layering follow beneath with horizontal layering beginning at 1.8 km depth at 4 km profile distance and at 1.9 km depth at 10 km profile distance. A layer of higher-amplitude parallel reflections is again visible above 2.2 km depth.

Shallow reflectivity structures can be linked to low-velocity zones in the upper 200 mbsf. These zones are aligned well with reflectivity patterns on both profiles. At profile P1 the extended low-velocity zone with increased velocities above for more than 4.5 km profile distance is related to high-reflectivity amplitudes at 1.8 km depth. The shallow strong-contrast anomaly at profile P2 is coincident in depth with a high-amplitude reflector. The reflector is visible along a wider area than the velocity structure. The transition in the inverted $v_P$ models to 2200 m/s at a depth of approximately 2.2 km is consistent with a change in reflectivity behavior at both profiles. All in all, a good agreement of migrated seismic images and inverted velocity models can be observed although zones recovered from FWI exhibit less horizontal continuity than expected from the reflection seismic result.

## ESTIMATION OF HYDRATE AND GAS SATURATION

To evaluate inverted parameter models in terms of potential hydrate and gas saturation we make use of an effective-medium approach using the P-wave modulus $M = \rho {v_P}^2$. We assume that the starting $v_P$ model and the derived density model represent water-saturated sediment. To describe the relation of the P-wave modulus of water saturated sediment $M_{sed}$ with the P-wave moduli of water $M_{fl}$ and of the sediment matrix $M_{sol}$ we use the Reuss average

$$\frac{1}{M_{sed}} = \frac{f_{fl}}{M_{fl}} + \frac{1 - f_{fl}}{M_{sol}} \tag{3}$$

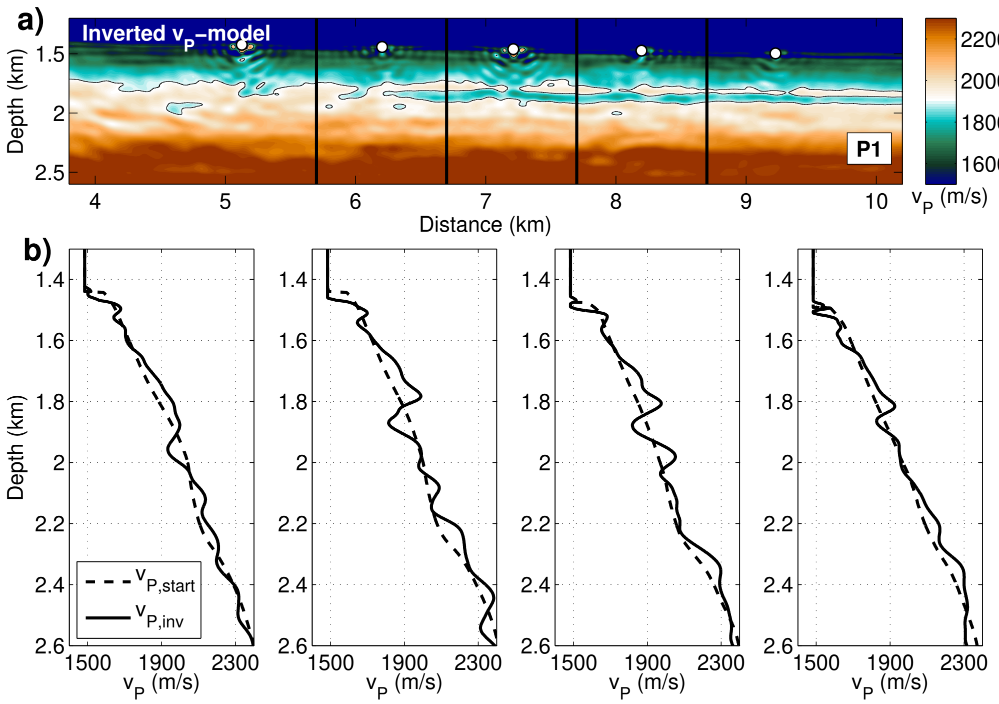


**Figure 8:** (a) Inverted $v_P$ model and (b) depth profiles for field data inversion of profile P1 using all events. An extended low-velocity zone underneath an increased-velocity layer is visble between 6.5 km and 10 km profile distance.

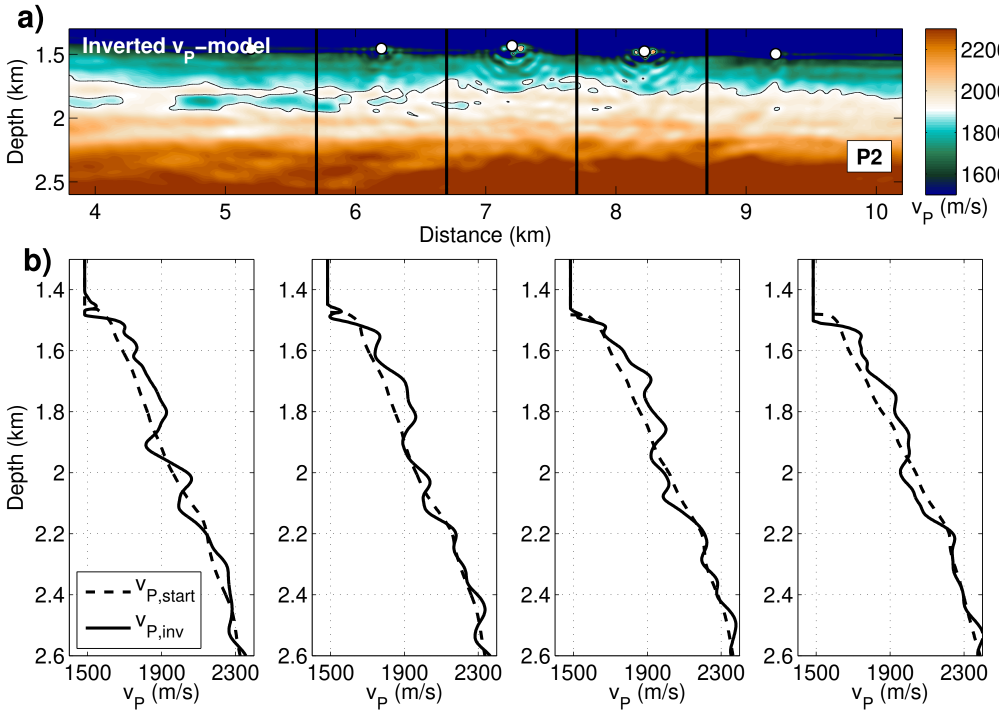


**Figure 9:** (a) Inverted $v_P$ model and (b) depth profiles for field data inversion of profile P2 using all events. A slight velocity increase can be observed at BSR depth (300 mbsf).

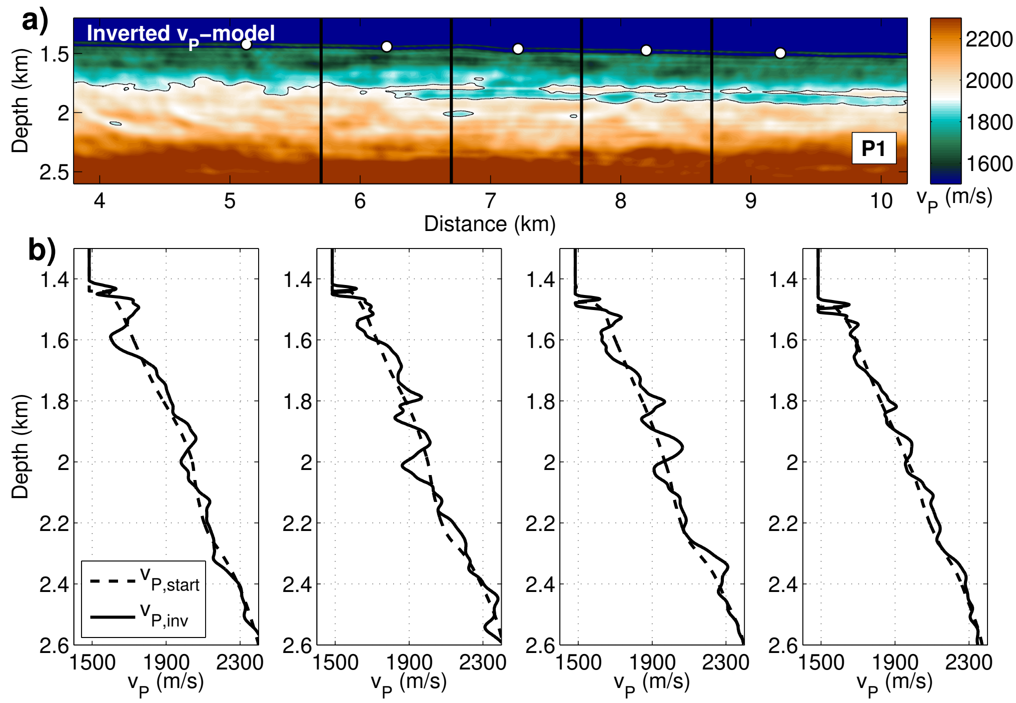


**Figure 10:** (a) Inverted $v_P$ model and (b) depth profiles for field data inversion of profile P1 using the muted input data. Additional shallow low velocity zones can be observed between 5.5 km and 8 km profile distance.

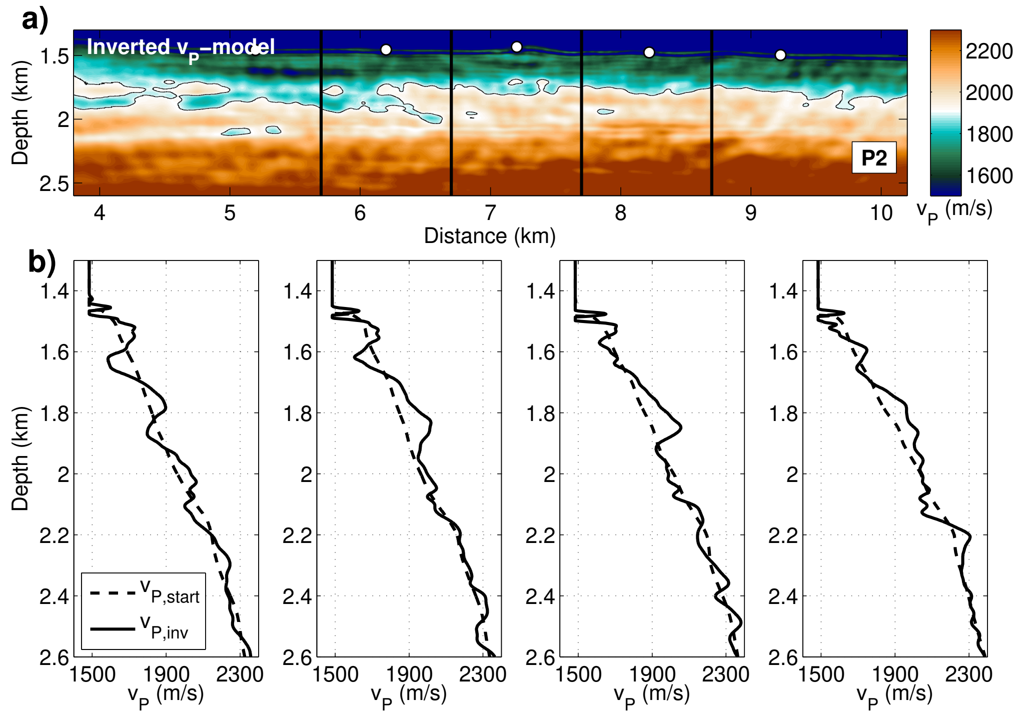


**Figure 11:** (a) Inverted $v_P$ model and (b) depth profiles for field data inversion of profile P2 using the muted input data. Shallow low-velocity zones are visible between 5 km and 6 km profile distance at 200 mbsf as well as between 7 km and 9 km at 100 mbsf.

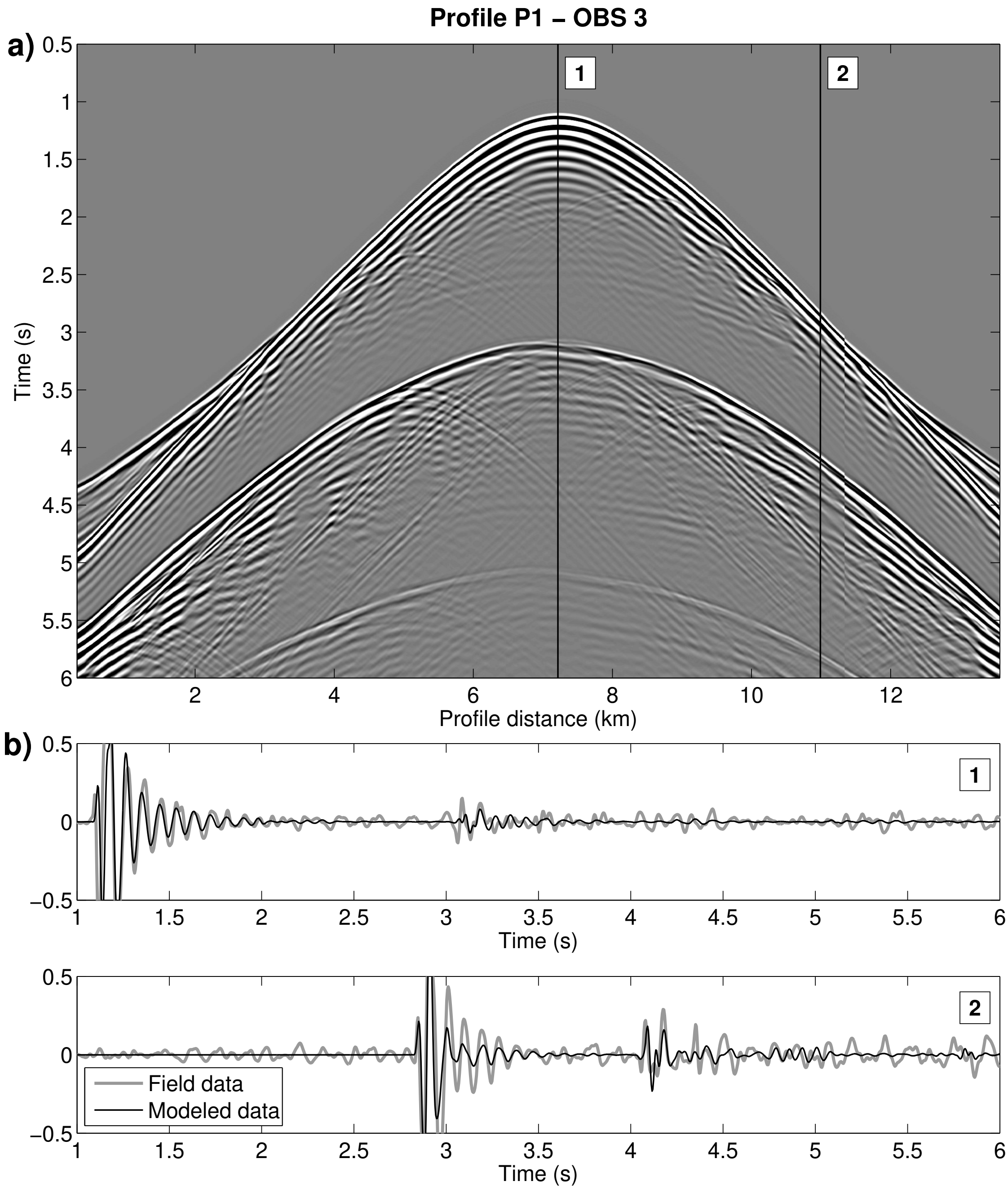


**Figure 12:** (a) Synthetic seismograms of OBS 3 for profile P1, (b) traces at 0 km (1) and 3.8 km (2) offset using all events.

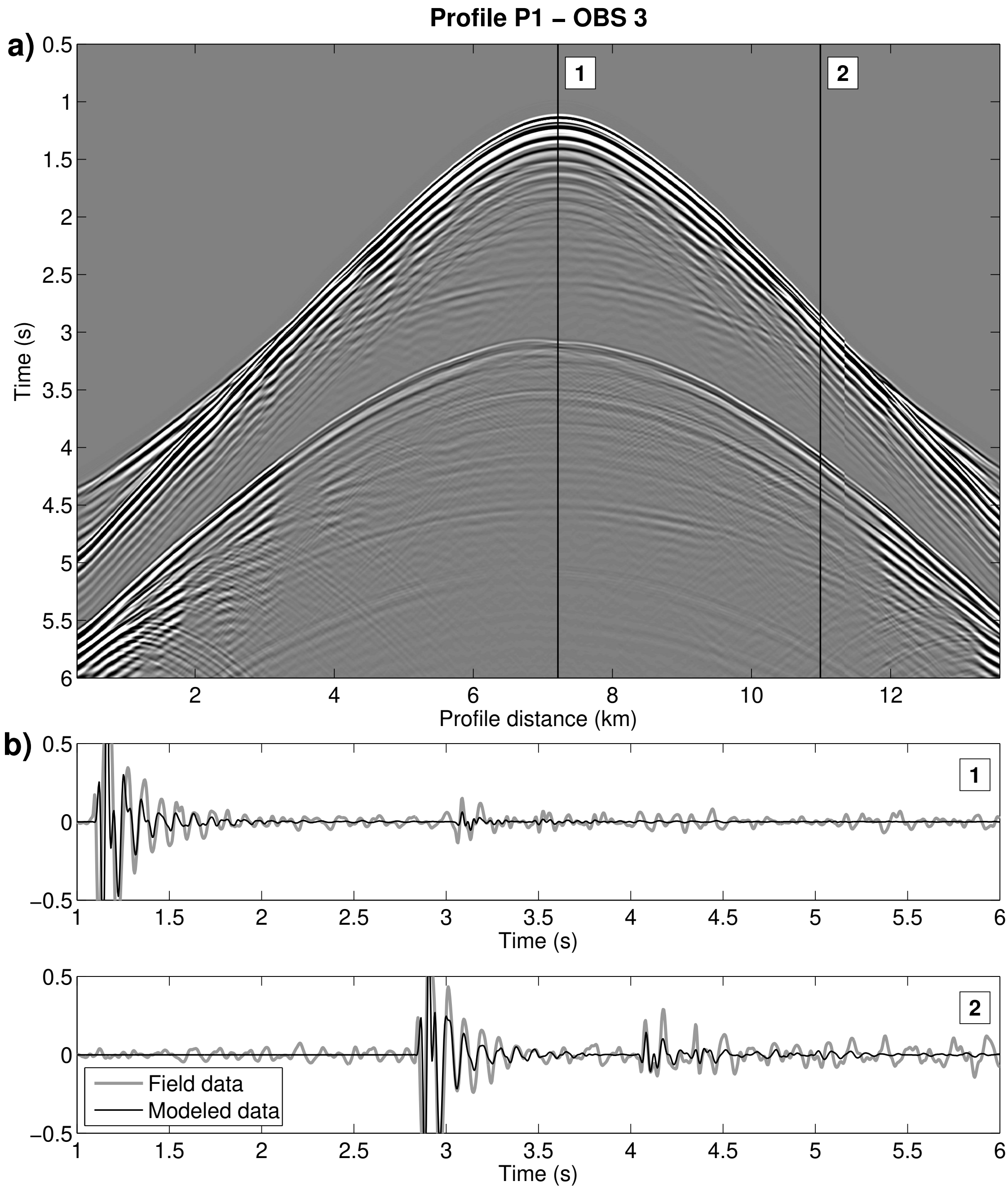


**Figure 13:** (a) Synthetic seismograms of OBS 3 for profile P1, (b) traces at 0 km (1) and 3.8 km (2) offset using the muted input data.

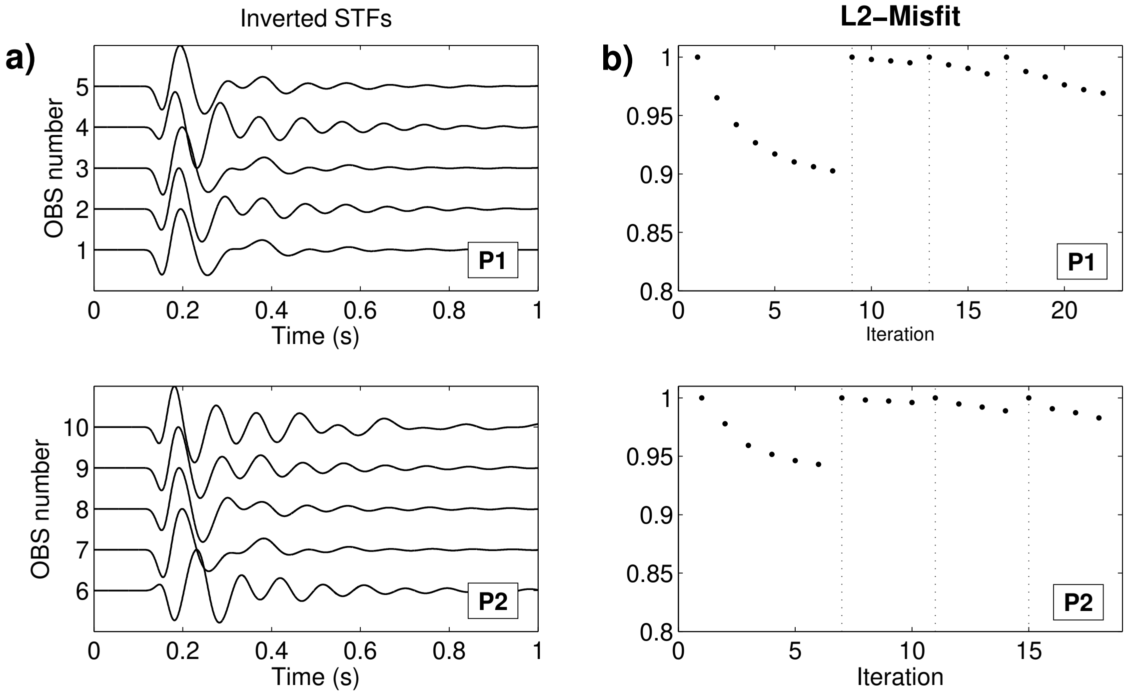


**Figure 14:** (a) Inverted STFs and (b) misfit curves of profiles P1 and P2 using all events.

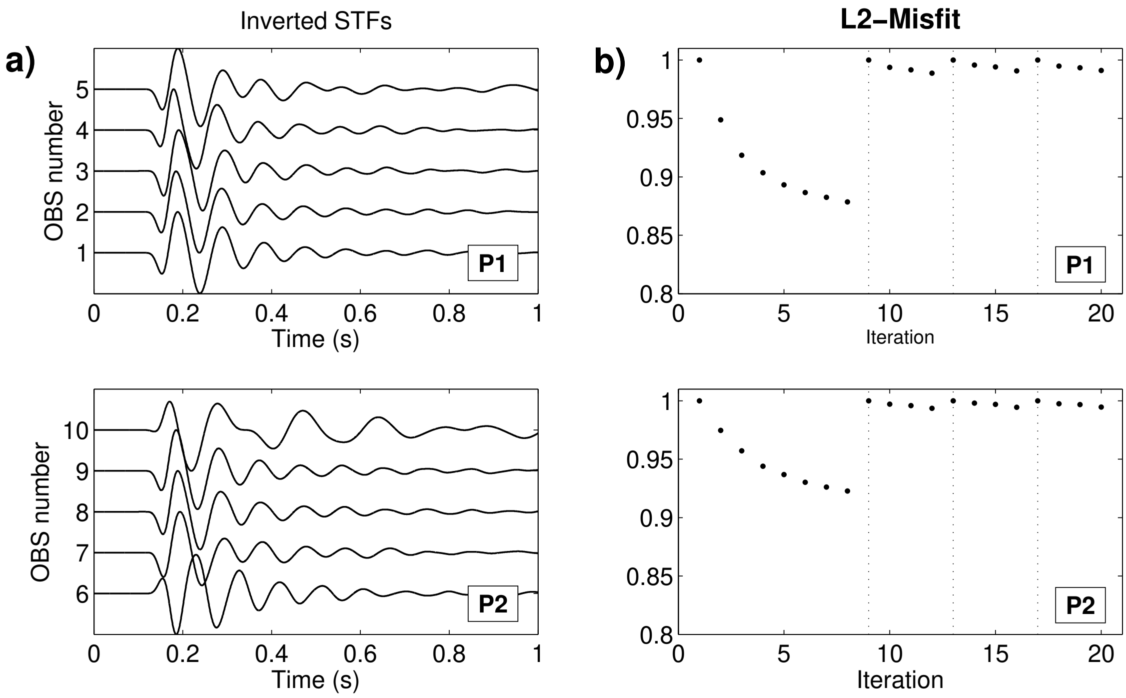


**Figure 15:** (a) Inverted STFs and (b) misfit curves of profiles P1 and P2 using the muted input data.

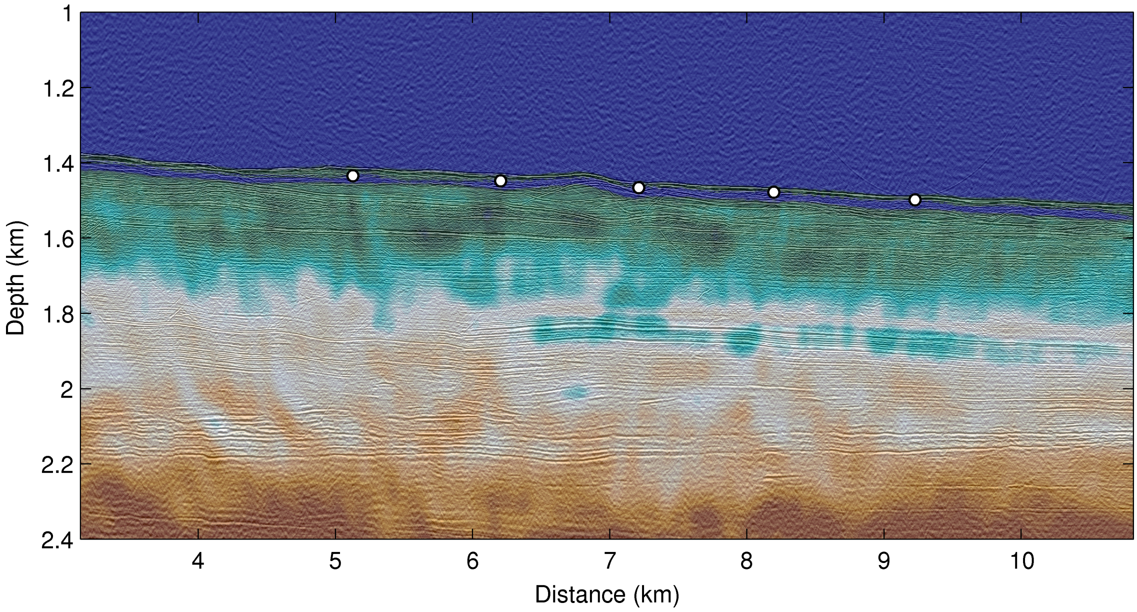


**(a)**

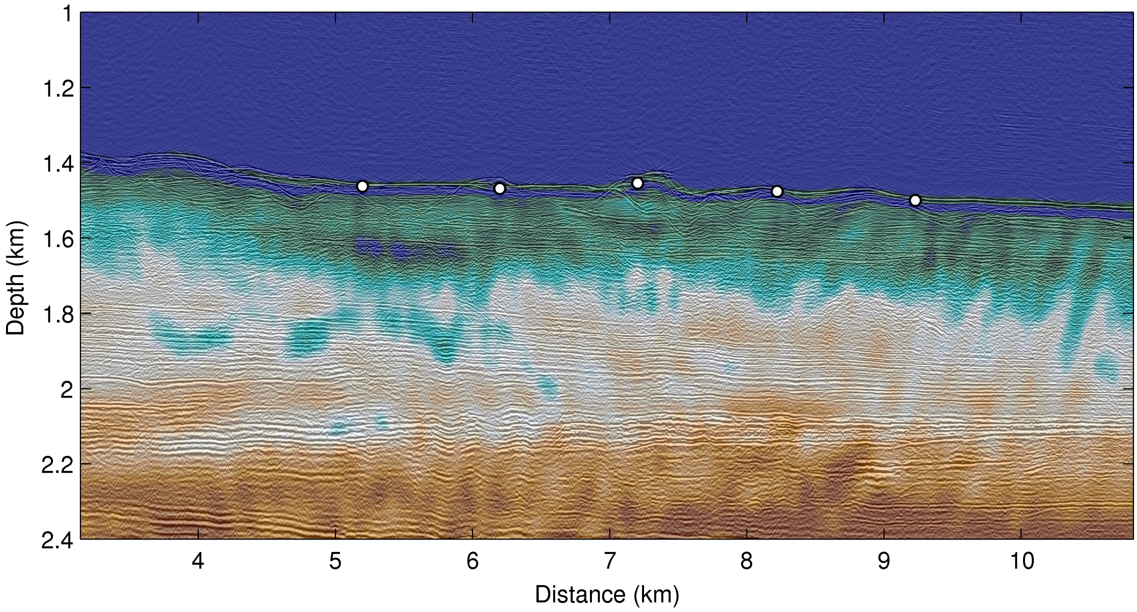


**(b)**

**Figure 16:** Overlay of inverted $v_P$ models from inversion of the muted input data of profile (a) P1 and (b) P2 with migrated seismic streamer data. The colorbar is the same as in Figures 8 to 11.

| | $M$ in GPa | $v_P$ in m/s | $\rho$ in kg/m$^3$ |
|---|---|---|---|
| Water | 2.25 | 1484 | 1020 |
| $CH_4$ gas | 0.11 | 412 | 230 |
| $CH_4$ hydrate | 12.8 | 3770 | 920 |
| Quartz | 96.6 | 6040 | 2650 |
| Clay | 30.0 | 3410 | 2580 |

**Table 1:** Parameters of sediment constituents after Carcione and Tinivella (2000); Helgerud et al. (2000); Waite et al. (2009) and references therein.

with the fraction of fluid $f_{fl}$, which gives a lower-bound estimate. Using literature values for the modulus of sea water and assuming an equal mix of the P-wave moduli of clay and quartz to calculate $M_{sol}$ (Table 1), we can estimate $f_{fl}$. It is then kept constant for further calculations. The inverted parameter models are then supposed to show the effect of hydrate or gas on $M_{fl}$ such that we have

$$M_{fl}^{*} = \frac{M_{h/g} M_{fl}}{S_{h/g} M_{fl} + \left(1 - S_{h/g}\right) M_{h/g}} \tag{4}$$

with $S_{h/g}$ representing hydrate or gas saturation of the pore fluid, respectively. This approach corresponds to the Wood equation discussed e.g. by Lee et al. (1996). Finally, we can calculate an estimate of hydrate or gas saturation by using starting and inverted parameter models of the FWI application. Effectively, we transfer a positive parameter update to hydrate and negative parameter changes to gas saturation. We limit potential hydrate occurrence to above and gas occurrence to the region below the interpreted BSR horizon, respectively.

With the assumed values shown in Table 1 we find that $f_{fl}$ decreases from 45 % at the seafloor to 15 % at the bottom of the model. The resulting saturation models show that we can estimate a hydrate saturation of up to 25 % at 7.5 km profile distance above the BSR at profile P1 (Figure 17). Below the BSR potential gas saturation reaches up to 1.2 % at 8 km. At profile P2 up to 28 % hydrate saturation at 4.8 km distance are reached above and 1.2 % at 4.8 km distance below the BSR, respectively (Figure 18). While in profile P1 the potential hydrate and gas zones are relatively continuous along the BSR, the distribution on profile P2 is patchy and below the BSR almost no indications for gas are present.

The absolute values of estimated saturation strongly depend on the assumed sediment composition and porosity values. Typically, gas saturation values are in the range of a few percent, independent of the approach. For a robust estimation of hydrate saturation further details on the subsurface composition, for example from borehole measurements are necessary.

## CONCLUSION

Synthetic studies show that a typical signature of hydrate and gas deposits which is most prominent in the $v_P$ model is well recoverable from an OBS data set with only few stations available. The application of 2D acoustic FWI to OBS hydrophone data of two parallel profiles from the Western Black Sea allows us to resolve detailed structures in the range of tens of meters and provides a consistent interpretation of potential hydrate and gas occurrence in the study area. The application of a time window suppressing the direct wave and primary reflections proves beneficial for the inversion. A reduction of artifacts close to the OBS locations resulting from deviations of the true instrument positions relative to their projection on the profile can be achieved. Furthermore, we judge that the application of muting of the direct wave and primary reflections as a valuable measure to give equal weight to the refracted wave portion and the reflected waves while reducing the influence of the high-amplitude direct wave signal which carries only limited information and conceals the following reflections. Because of the similar wave paths of the multiple reflections no significant information is lost by removing the primary reflections.

The obtained velocity structures in $v_P$ from field-data inversion can be related to reflectivity behavior visible in the migrated seismic data. A typical $v_P$ distribution as expected for hydrate and gas occurrence is observed on profile P1 with elevated velocities above the interpreted BSR line appearing together with an extended low-velocity zone. The zone of reduced velocity is coincident with high-reflectivity amplitudes in

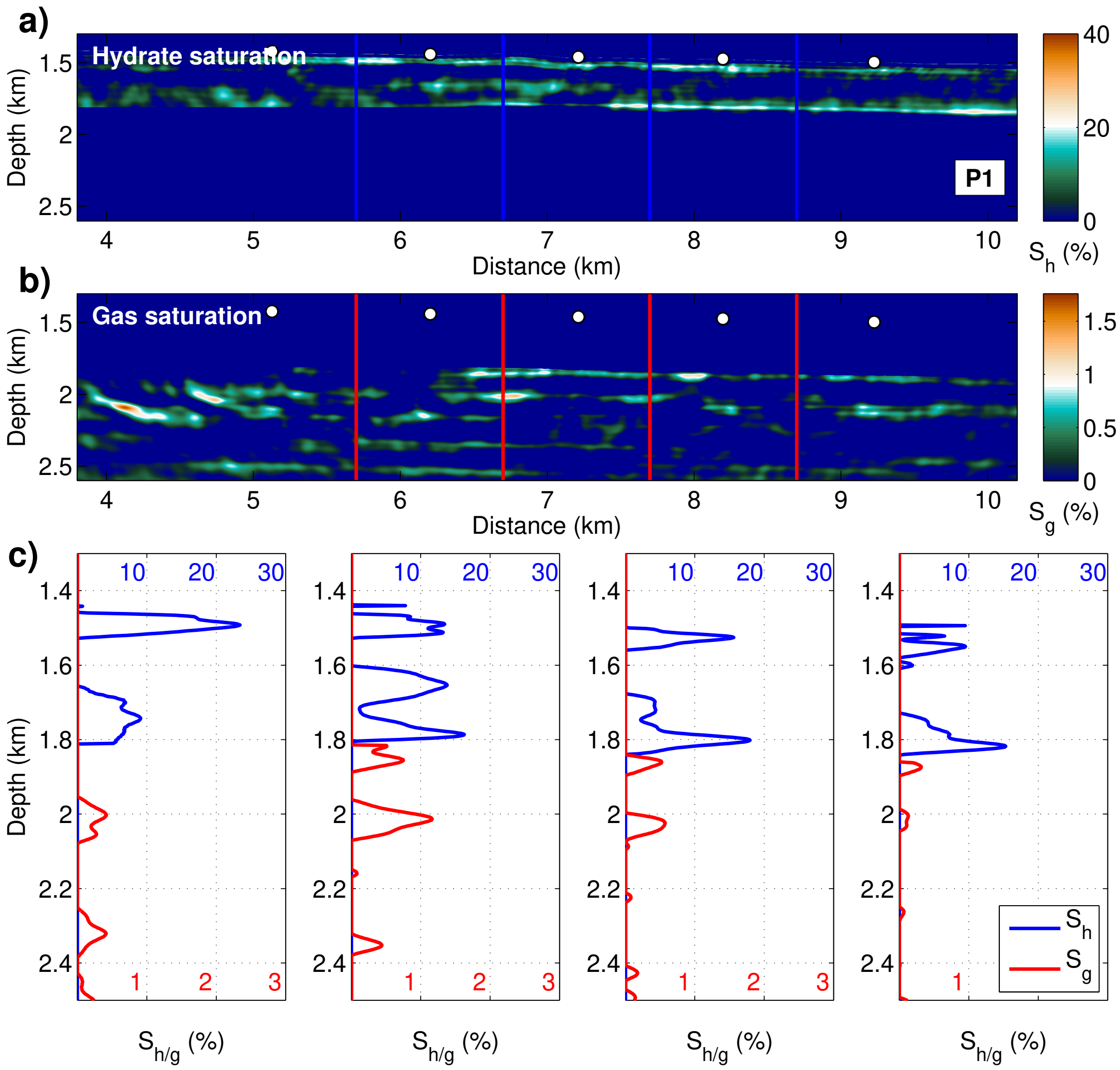


**Figure 17:** (a) Estimated hydrate and (b) gas saturation for profile P1 from inversion of the reduced signal content. (c) Depth profiles show estimated saturations at the same locations as in Figure 10.

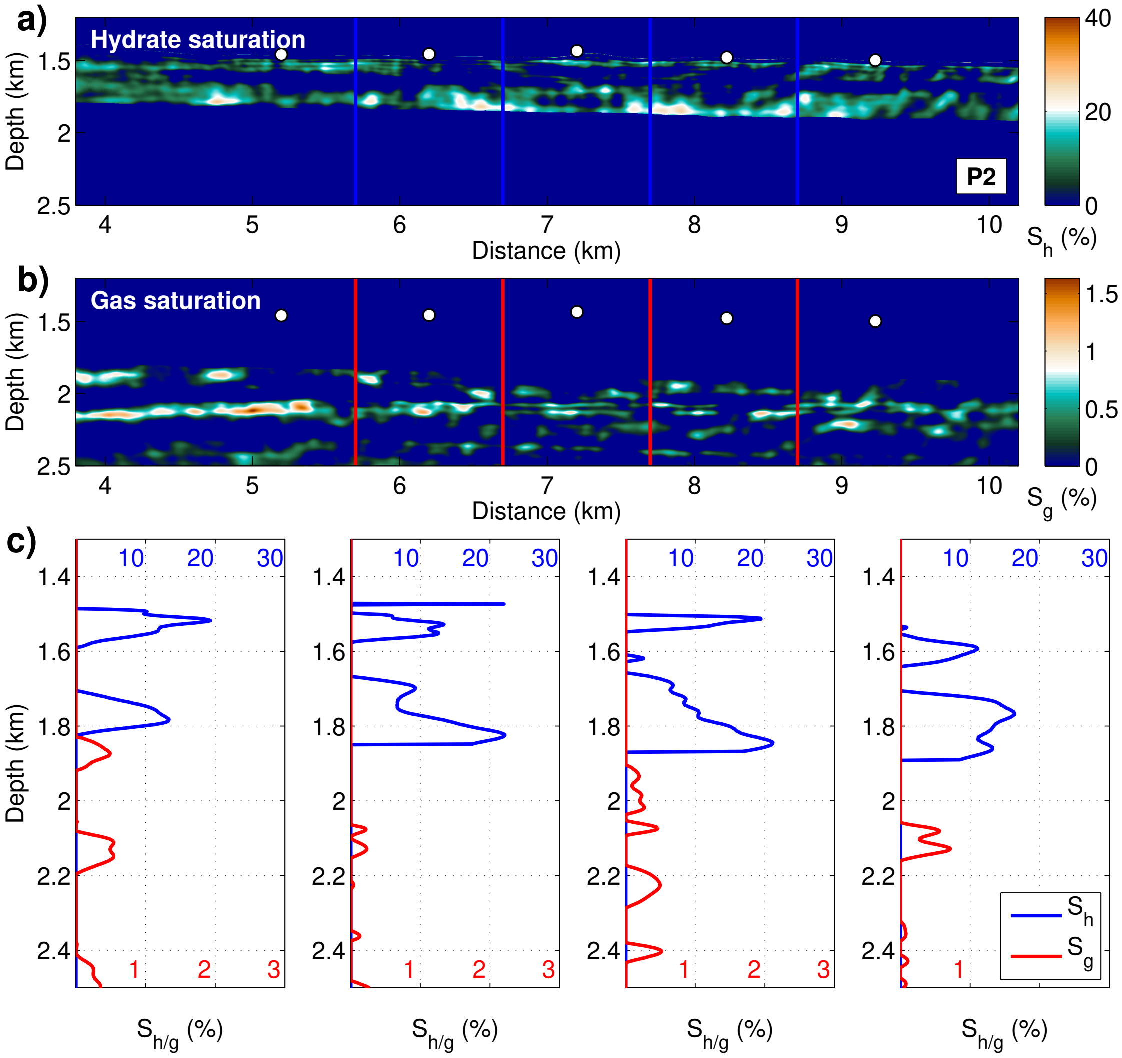


**Figure 18:** (a) Estimated hydrate and (b) gas saturation for profile P2 from inversion of the reduced signal content. (c) Depth profiles show estimated saturations at the same locations as in Figure 11.

the migrated seismic section. While increased velocities are visible above BSR depth on profile P2, below the BSR no velocity decrease is constructed by the inversion indicating that no gas is present below the observed horizon.

## ACKNOWLEDGMENTS

We thank Anke Dannowski (GEOMAR) for providing the OBS traveltime tomography models used as starting models for FWI, and Timo Zander (GEOMAR) for supplying migrated seismic sections and interpretations. This work was carried out in the framework of the SUGAR-III project funded by BMWi (grant number 03SX381C) and kindly supported by the sponsors of the Wave Inversion Technology (WIT) consortium. The authors gratefully acknowledge the computing time granted on the supercomputer JURECA at Juelich Supercomputing Centre (JSC) and ForHLR I and II at the Karlsruhe Institute of Technology (KIT).

## PUBLICATION

This WIT article was submitted for publication in *Geophysics*.

## REFERENCES

Bialas, J., Klaucke, I., and Haeckel, M. (2014). FS MARIA S. MERIAN Fahrtbericht/Cruise Report MSM34/1 & 2-SUGAR Site; Varna–Varna, 06.12.13–16.01.14.

Bohlen, T. (2002). Parallel 3-D viscoelastic finite difference seismic modelling. *Computers & Geosciences*, 28(8):887–899.

Carcione, J. M. and Tinivella, U. (2000). Bottom-simulating reflectors: Seismic velocities and AVO effects. *Geophysics*, 65(1):54–67.

Choi, Y. and Alkhalifah, T. (2012). Application of multi-source waveform inversion to marine streamer data using the global correlation norm. *Geophysical Prospecting*, 60(4):748–758.

Delescluse, M., Nedimović, M. R., and Louden, K. E. (2011). 2D waveform tomography applied to long-streamer MCS data from the Scotian Slope. *Geophysics*, 76(4):B151–B163.

Forbriger, T., Groos, L., and Schäfer, M. (2014). Line-source simulation for shallow-seismic data. Part 1: Theoretical background. *Geophysical Journal International*, 198(3):1387–1404.

Gardner, G., Gardner, L., and Gregory, A. (1974). Formation velocity and density - The diagnostic basics for stratigraphic traps. *Geophysics*, 39(6):770–780.

Groos, L., Schäfer, M., Forbriger, T., and Bohlen, T. (2014). The role of attenuation in 2D full-waveform inversion of shallow-seismic body and Rayleigh waves. *Geophysics*, 79(6):R247–R261.

Guerin, G. and Goldberg, D. (2002). Sonic waveform attenuation in gas hydrate-bearing sediments from the Mallik 2L-38 research well, Mackenzie Delta, Canada. *Journal of Geophysical Research: Solid Earth*, 107(B5).

Helgerud, M. B., Dvorkin, J., and Nur, A. (2000). Rock physics characterization for gas hydrate reservoirs: Elastic properties. *Annals of the New York Academy of Sciences*, 912(1):116–125.

Jaiswal, P., Dewangan, P., Ramprasad, T., and Zelt, C. (2012). Seismic characterization of hydrates in faulted, fine-grained sediments of Krishna-Godavari Basin: Full waveform inversion. *Journal of Geophysical Research: Solid Earth (1978–2012)*, 117(B10).

Kim, H.-J., Jou, H.-T., Kang, S.-G., Lee, G. H., Yi, B. Y., Yoo, D.-G., Ryu, B.-J., and Shin, C. (2013). Seismic characterization and imaging of a gas hydrate deposit in the western part of the Ulleung Basin, the East Sea (Japan Sea). *Marine and Petroleum Geology*, 47:214–221.

Köhn, D. (2011). *Time domain 2D elastic full waveform tomography*. PhD thesis, Christian-Albrechts-Universität zu Kiel.

Korenaga, J., Holbrook, W., Singh, S., and Minshull, T. (1997). Natural gas hydrates on the southeast US margin: Constraints from full waveform and travel time inversions of wide-angle seismic data. *Journal of Geophysical Research: Solid Earth (1978–2012)*, 102(B7):15345–15365.

Kurzmann, A. (2012). *Applications of 2D and 3D full waveform tomography in acoustic and viscoacoustic complex media*. PhD thesis, Karlsruhe Institute of Technology.

Kvenvolden, K. A. (1993). Gas hydrates - geological perspective and global change. *Reviews of Geophysics*, 31(2):173–187.

Lee, M., Hutchinson, D., Collett, T., and Dillon, W. P. (1996). Seismic velocities for hydrate-bearing sediments using weighted equation. *Journal of Geophysical Research: Solid Earth*, 101(B9):20347–20358.

Mora, P. (1988). Elastic wave-field inversion of reflection and transmission data. *Geophysics*, 53(6):750–759.

Pecher, I. A., Minshull, T. A., Singh, S. C., and von Huene, R. (1996). Velocity structure of a bottom simulating reflector offshore Peru: Results from full waveform inversion. *Earth and Planetary Science Letters*, 139(3):459–469.

Plessix, R.-E. (2006). A review of the adjoint-state method for computing the gradient of a functional with geophysical applications. *Geophysical Journal International*, 167(2):495–503.

Plessix, R.-E. and Mulder, W. (2004). Frequency-domain finite-difference amplitude-preserving migration. *Geophysical Journal International*, 157(3):975–987.

Sears, T. J., Singh, S., and Barton, P. (2008). Elastic full waveform inversion of multi-component OBC seismic data. *Geophysical Prospecting*, 56(6):843–862.

Singh, S. C., Minshull, T. A., and Spence, G. D. (1993). Velocity structure of a gas hydrate reflector. *Science*, 260:204–207.

Tarantola, A. (1984). Inversion of seismic reflection data in the acoustic approximation. *Geophysics*, 49(8):1259–1266.

Virieux, J. (1986). P-SV wave propagation in heterogeneous media: Velocity-stress finite-difference method. *Geophysics*, 51(4):889–901.

Virieux, J. and Operto, S. (2009). An overview of full-waveform inversion in exploration geophysics. *Geophysics*, 74(6):WCC1–WCC26.

Waite, W. F., Santamarina, J. C., Cortes, D. D., Dugan, B., Espinoza, D., Germaine, J., Jang, J., Jung, J., Kneafsey, T. J., Shin, H., et al. (2009). Physical properties of hydrate-bearing sediments. *Reviews of Geophysics*, 47(4).

Zander, T., Haeckel, M., Berndt, C., Chi, W.-C., Klaucke, I., Bialas, J., Klaeschen, D., Koch, S., and Atgın, O. (2017). On the origin of multiple BSRs in the Danube deep-sea fan, Black Sea. *Earth and Planetary Science Letters*, 462:15–25.